

Numerical modelling of medical ultrasound: phantom-based verification

Yu. V. Vassilevski^{*†‡}, K. A. Beklemysheva^{†*}, G. K. Grigoriev[§], N. S. Kulberg[¶],
I. B. Petrov^{†*}, and A. V. Vasyukov[†]

Abstract — The paper is devoted to verification of previously proposed technique of medical ultrasound modelling [3]. A medical phantom was used as an object with well documented geometry and mechanical properties. The comparison of simulation results with raw data from ultrasound scanner is presented. A virtual B-scan is also obtained and compared with an experimental image.

Keywords: Medical ultrasound, grid-characteristic method, model verification.

MSC 2010: 65M25

Ultrasonography is one of the most reliable and accessible diagnostic procedures, it is commonly used in medical practice. Numerical modelling of medical ultrasound has a few decades of history, numerous governing equations and algorithms have been developed [6]. However, this area of research offers several open problems. One of the problems is transcranial scanning with skull-induced signal aberrations.

Several research studies addressed related problems. The paper [1] is devoted to therapeutic transcranial ultrasound and covers the issues similar to our research. However, the therapeutic ultrasound is based on an ultrasound system coupled with magnetic resonance imaging scanner. This multimodality imaging system allows one to use high-resolution brain tomographic images for ultrasound navigation. The paper [7] studies transcranial ultrasound propagation and skull-induced aberration correction techniques. The motivation of the study is the usage of the focused ultrasound for neurosurgical interventions, and the proposed method relies on tomographic data. Our research is focused on diagnostic usage of ultrasound. In this case magnetic resonance imaging or computed tomography is impractical due to its cost.

A new concept for numerical modelling of ultrasound scanning of biological

^{*}Institute of Numerical Mathematics of the RAS, 8 Gubkina str., Moscow 119333. E-mail: yuri.vassilevski@gmail.com

[†]MIPT, 9 Institutskiy per., Dolgoprudny 141700, Moscow Region

[‡]Sechenov University, 2-4 Bolshaya Pirogovskaya str., Moscow 119991, Russia

[§]MGTS Medical and Health Center, Petrovsky blvd., 12, bld. 1, Moscow 127051, Russia

[¶]Moscow Scientific and Practical Center of Medical Radiology, Srednaya Kalitnikovskaya str., 28, bld. 1, Moscow 109029; IEI FRC CSC RAS, Vavilov str., 44, block 2, Moscow 119333, Russia

The research was supported by the Russian Science Foundation grant 14-31-00024.

objects was presented by the authors in [3]. The paper was focused on the development of a modelling technique for ultrasound propagation in heterogeneous medium featuring contacts between tissues with significantly different mechanical properties and complicated contact surfaces.

The primary objective of the present paper is a verification of the numerical model [3] for diagnostic ultrasound by means of direct comparisons of numerical and experimental data.

The structure of the paper is as follows. In Section 1 we present governing equations for wave propagation phenomena and discuss features of the numerical model allowing to take into account scattered echoes correctly. Section 2 describes the experimental setup which includes a medical phantom, properties of the scanning signal, a format of raw data used for the direct comparison and verification. The simulation results and the comparison of numerical and experimental data are presented and discussed in Section 3. Section 4 contains a few closing remarks.

1. Ultrasound propagation model

1.1. Governing equations and discretization

Our numerical model is based on acoustic equations. Ultrasound pulse propagation is described by the following system of partial differential equations:

$$\begin{aligned} \rho(\mathbf{x}) \frac{\partial \mathbf{v}(\mathbf{x}, t)}{\partial t} + \nabla p(\mathbf{x}, t) &= 0 \quad \text{in } \Omega \\ \frac{\partial p(\mathbf{x}, t)}{\partial t} + \rho(\mathbf{x}) c^2(\mathbf{x}) \nabla \cdot \mathbf{v}(\mathbf{x}, t) &= -\alpha(\mathbf{x}) c(\mathbf{x}) p(\mathbf{x}, t) \quad \text{in } \Omega \end{aligned} \quad (1.1)$$

where Ω is the domain occupied by the medium, \mathbf{x} is the point in Ω , $\rho(\mathbf{x})$ is the density, $\mathbf{v}(\mathbf{x}, t)$ is the velocity vector, $p(\mathbf{x}, t)$ is the acoustic pressure, $c(\mathbf{x})$ is the speed of sound, $\alpha(\mathbf{x})$ is the attenuation coefficient of the Maxwell model [9].

Equations (1.1) are completed by Dirichlet boundary conditions:

$$p|_{\partial\Omega} = p^* \quad \text{on } \partial\Omega. \quad (1.2)$$

Inhomogeneous Dirichlet boundary condition is used to model a transmitter acting on a part of the domain boundary. Homogeneous Dirichlet boundary condition $p^* = 0$ on the rest of $\partial\Omega$ means a free boundary.

The model takes into account longitudinal (pressure) waves in tissues and does not describe transverse (shear) waves. Such simplification makes sense since the attenuation coefficient for the shear waves is four orders of magnitude greater than that for the pressure waves at frequencies from MHz range [4, 8].

The numerical solution of (1.1) is obtained by the method of characteristics described in [3].

1.2. Modelling scattered echoes

We distinguish two types of ultrasound response in biological tissues. The *specular* response is caused by echoes originating from relatively large, regularly shaped inclusions with smooth interfaces [12]. These echoes correspond to the reflection from interfaces between tissues with different mechanical properties. Such echoes are relatively intense and angle-dependent. A computational mesh should recover the reflecting inclusions. Modelling of these echoes was described in detail in our previous work [3].

The *scattered* response is generated by echoes from relatively small, weakly reflective, irregularly shaped inclusions [12]. These echoes correspond to the reflections from blood cells and similar tiny objects. Such echoes are less intense and less sensitive to the angle of scanning. In medical practice, the scattered echoes encode valuable information and form a significant part of the observed medical images. Importance of scattered echoes is evident on B-scans of medium containing cavities filled with homogeneous fluid (Fig. 8a). Unless raw data of the receiver contain the scattered echoes, the cavities are not detected (compare Figs. 8c and 8d). The detailed analysis of Fig. 8 is given in Section 3.

In numerical simulation, the explicit resolution of tiny reflecting inclusions on a computational mesh for examined tissues is impractical due to unrealistic demands of computing resources. We suggest a different approach to modelling of scattered echoes. Each tiny reflecting inclusion is added atop of the computational mesh as the pair (\mathbf{x}, s) , where \mathbf{x} designates the inclusion position and s denotes the relative reflection intensity coefficient. Exact numbers of such reflectors in medical phantoms are not presented in the literature. In our numerical experiment we distributed $2 \cdot 10^4$ reflectors over the medium. The overall scattered response is calculated by the following strategy. The propagation of the initial acoustic pulse through the medium is modelled by the method of characteristics as described in [3]. If the initial pulse reaches a point where a tiny reflector resides, then an effective reflected wave is formed at that point. The effective echo from a tiny reflector is represented by for-

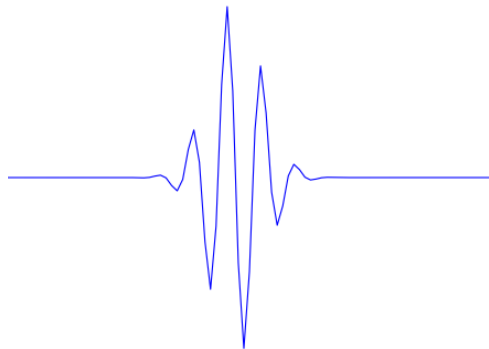


Figure 1. Echo from a tiny reflector.

mula:

$$p_r = p_i s e^{-t^2/2\tau^2} \cos(\omega t) \quad (1.3)$$

where t is the time, p_r is the amplitude of the reflected wave, p_i is the amplitude of the initial pulse at the point where the reflector resides, parameter s is the reflection intensity coefficient for the reflector, parameter ω is the carrier frequency, parameter τ depends on the transmitter size and the speed of sound. Note that the attenuation is not taken into account explicitly in this formula for reflected signal, since it is included into the governing equation for the pulse propagation in the medium.

A typical form of the echo from a tiny reflector is presented in Fig. 1.

The propagation of each scattered echo in the medium is computed by the ray tracing technique which applies the shooting method to the initial value problem. In case of scattered echoes, the speed of sound is constant in the medium, therefore the ray tracing reduces to a simple version of the universal technique [10]. The scattered response is computed in the following steps:

1. When the initial pulse reaches a tiny inclusion, the effective echo (1.3) from this inclusion is generated.
2. Since the speed of sound is constant, the ray path from the echo source (the inclusion) to the receiver is given by a straight line.
3. When the echo reaches the receiver, it is recorded for further processing.
4. The echoes from different inclusions propagate independently. The overall scattered response from the medium with background reflectors is registered with delays accounting propagation of echoes from the tiny reflectors to the receiving elements.

The numerical model of the signal propagation does not take into account the secondary reflection: only the initial acoustic pulse from the transmitter interacts with the tiny inclusions and initiates the scattered response. The echo reflected from a tiny reflector does not interact with other inclusions. This approach is based on the fact that scattered echoes are one order of magnitude less intense than the initial pulse.

2. Experiment setup

2.1. Signal characteristics

For verification of our model we used an experimental setup with ATL Ultramark 7 ultrasound system. The system has 8 bit analog-to-digital converter with sampling frequency 12 MHz and a sector phased array containing 48 elements.

The signal transmitted by each element has the following form:

$$p(\mathbf{x}, t) = p_0 \int_{\omega_0 - \Delta\omega}^{\omega_0 + \Delta\omega} e^{-i(\omega t - \mathbf{k}\mathbf{x})} d\omega. \quad (2.1)$$

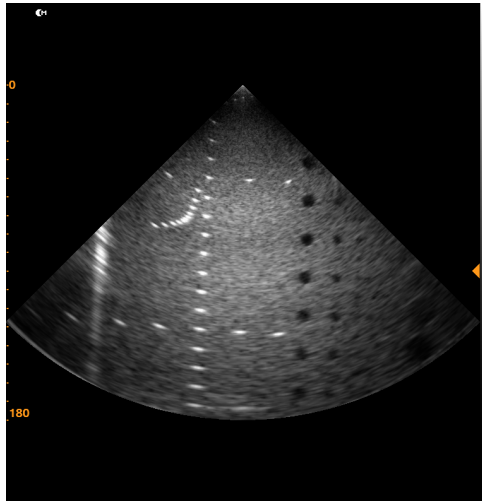


Figure 2. Phantom structure: thin pins (white points), cavities with fluid (black circles).

In this equation ω is the frequency, \mathbf{k} is the wave vector, ω_0 is the transmitter base frequency, $\Delta\omega$ is determined by transmitter characteristics, p_0 is the amplitude which is independent of the frequency. In our measurements, the transmitted signal had the base frequency $\omega_0 = 3$ MHz and $\Delta\omega = 1$ MHz.

2.2. Phantom

The verification of the numerical model was performed on the basis of the medical phantom [5]. Phantoms are heterogeneous media with documented geometrical and mechanical characteristics, that are used to configure an ultrasonic equipment. The bulk of the phantom is a homogeneous substance (e.g., a transparent polymer) with acoustic properties corresponding to the properties of human tissues in terms of the speed of sound and the attenuation coefficients. The latter can be modified by varying the concentration of tiny inclusions made of a rheologically contrast material.

The structure of the phantom used in the verification is presented in Fig. 2. White points correspond to thin pins (0.1 mm in diameter), black circles are cavities (10 mm in diameter) filled with fluid, the bulk of the phantom is filled with a human tissue mimicking gel. The speed of sound in the gel is 1500 m/s.

The pins are rheologically contrast and produce bright echoes. The gel is filled with background tiny reflectors, the response from each individual reflector is an order of magnitude less intensive compared with the response from a pin. The fluid does not contain reflectors, thus it does not produce scattered echoes.

2.3. Raw data from ultrasound scanner

Obtaining raw data from an ultrasound scanner is a non-trivial task. The equipment typically provides access to processed B-scan only. In our case, the experimental

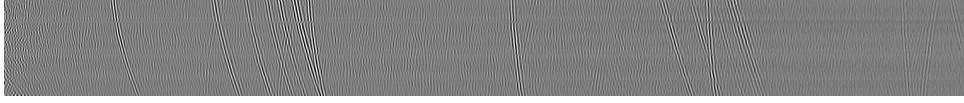


Figure 3. Raw data sample: an element of the phased array transmits the initial pulse, all elements of the phased array receive echoes. Each horizontal row of pixels represents recorded signal amplitude at a receiving element.

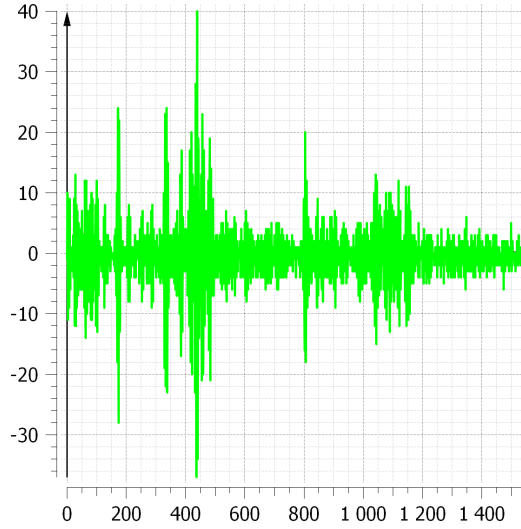


Figure 4. Raw data sample: an element of the phase array transmits the initial pulse, another element receives the echo.

raw data was recorded as follows: (a) Each single element of the phased array transmits the initial impulse independently. The transmitter generates 48 series of data, one for each element of the phased array. While an element transmits the pulse, the other elements are not active; (b) Recording starts immediately after the transmission ends and lasts $2z_{\max}/c$ seconds, where $z_{\max} = 10$ cm is the target depth of scanning in this experiment; (c) Each element of the phased array records echoes independently. This gives 48 curves for each transmitter. Each curve represents the signal amplitude on a receiving element as a function of time. The signal is digitized at 12 MHz frequency.

The described procedure generates 48 series of data, an example of data is presented in Fig. 3. Each horizontal row of pixels represents time dependence of the signal amplitude recorded at a receiving element. The number of pixels in the row is the number of records at the receiver obtained at 12 MHz frequency. Gray-scale intensity of each pixel encodes the amplitude of the signal.

Time-dependent signal amplitude may be presented in the conventional mode shown in Fig. 4. However, in this case $48 \times 48 = 2304$ 1D curves are needed for representation of the complete experimental dataset. For the sake of compactness, in our analysis of the row data we prefer to use 48 2D data samples similar to Fig. 3.

3. Comparison of numerical and experimental data

The numerical model reproduces the same setup that is used in the experiment presented in Section 3.

A quasiuniform tetrahedral mesh with $1.2 \cdot 10^6$ cells was used in our simulations (size of the mesh cell is about 1 mm). The mesh does not recover small reflecting objects (the pins and background tiny reflectors in the gel), their response was reproduced within the scattered reflection concept.

Indeed, the response from the pin is just a bright scattered echo from a tiny reflector with relatively large amplitude. The scattered response from $2 \cdot 10^4$ tiny reflectors forms a noisy grayscale background of the image. The cavity filled by fluid without tiny reflectors is visible as a dark circle on the resulting B-scan image.

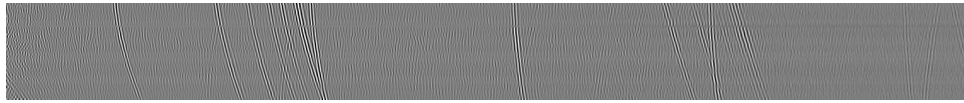
One simulation run takes 90 minutes on 4 core 64 bit workstation. About 90-95% of the computational time is spent to ray tracing that calculates the scattered response.

The results of the numerical modelling were encoded in the format of the experimental raw data that allows us to compare them directly. Figures 5, 6, and 7 represent echoes recorded by all receivers when the first, the middle, and the last element of the phased array, respectively, acted as the transmitter. The similar pictures were obtained for all transmitting elements. The most notable features on these pictures are oblique lines caused by the reflection from the thin pins of the phantom.

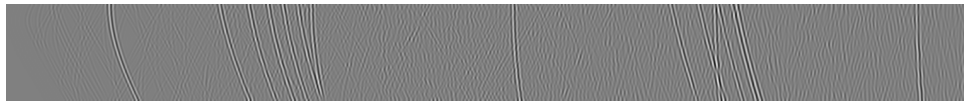
Also, we reconstructed the B-scan from the numerical data. The difficulty of the B-scan recovery is the lack of a detailed documentation on signal processing in the ultrasound scanner. We could only assume certain processing steps which result in the observed B-scan. Moreover, different data processing options lead to different brightness and contrast levels, and exact pixelwise coincidence between experimental and numerical B-scans can not be expected.

We used the following postprocessing pipeline to build the numerical B-scan from the simulated raw sensor data:

1. Generation of data frames that simulate the ultrasound beam focusing consequently in all the directions that sweep the area under examination. The scanning gap is 120 degrees, the number of rays is 230. It is achieved by summation of raw data with necessary delays. For each direction, we obtain a pixel array, where the number of pixel rows is equal to the number of receiving sensor elements. Each pixel row is obtained by the addition of rows from all generated raw data frames (one for each receiving element) with corresponding delays. The delays for transmitter index and receiver index are summed.
2. Generation of the B-scan. Each B-scan line corresponds to a beam in certain direction and is obtained by the addition of all the rows in the pixel array.
3. Narrowband filtering is applied to all lines of B-scan to reduce the noise and increase the quality of the Hilbert transform [2] at the next step. These filters are applied to the B-scan instead of raw data frames to speed up the process.

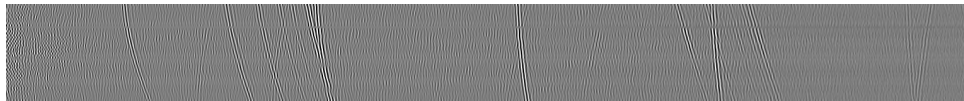


(a)

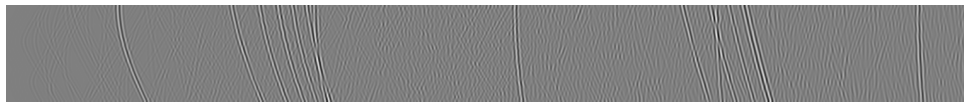


(b)

Figure 5. Comparison of raw data when the first element of the phased array transmits the pulse: experimental data (a), numerical data (b).

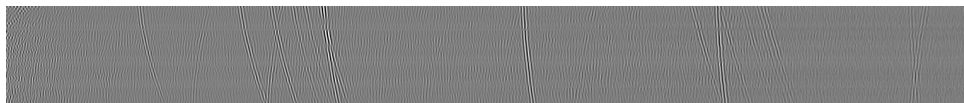


(a)

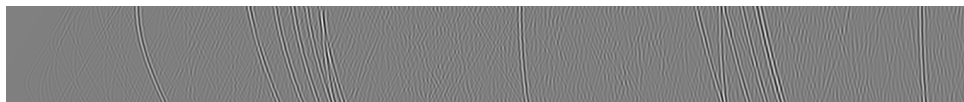


(b)

Figure 6. Comparison of raw data when the middle element of the phased array transmits the pulse: experimental data (a), numerical data (b).



(a)



(b)

Figure 7. Comparison of raw data when the last element of the phased array transmits the pulse: experimental data (a), numerical data (b).

4. The Hilbert transform is applied in order to obtain the signal envelope and eliminate the carrier frequency [11].
5. A transformation into the sector view is performed.

The result of the B-scan processing is presented in Fig. 8. Figure 8a presents the B-scan reconstructed on the ultrasound equipment from the experimental raw

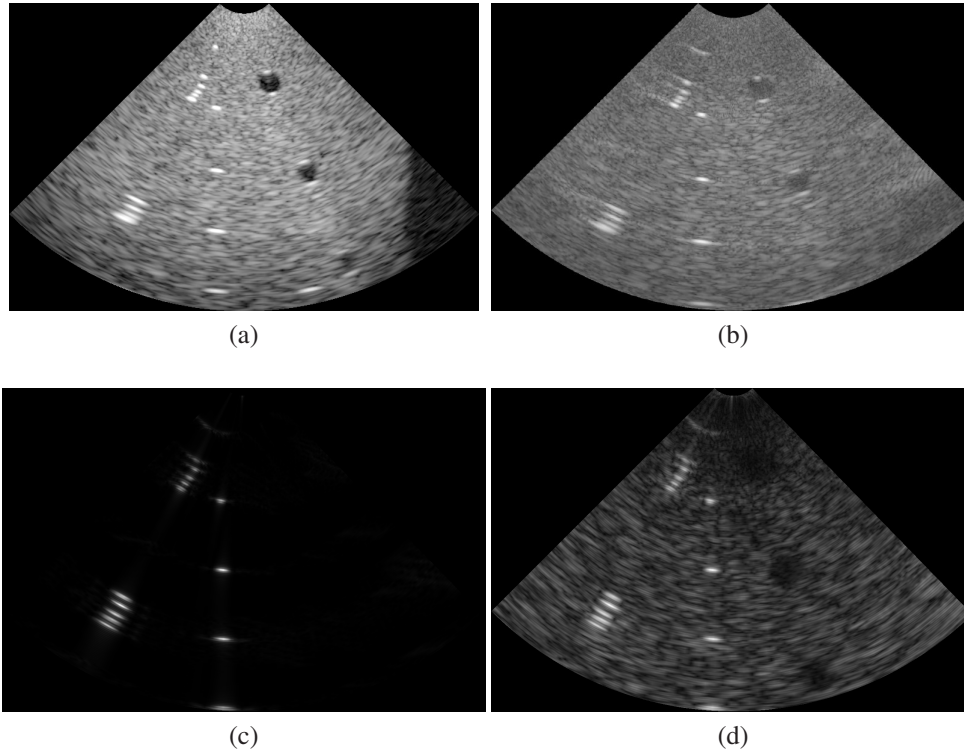


Figure 8. B-scan reconstructed on the ultrasound equipment (a), B-scan reconstructed by the numerical postprocessing of the experimental raw data (b), B-scan reconstructed by the numerical postprocessing of the simulated raw data which account bright pins only (c), B-scan reconstructed by the numerical postprocessing of the simulated raw data which account both pins and background reflectors in the gel (d).

data. The most notable features in this picture are the pins visible as white dots, the cavities filled with a homogeneous fluid visible as dark circles with bright specular echoes at their tops and bottoms, and the speckled grey background that emphasizes dark areas [5].

Figure 8b presents the B-scan reconstructed by the numerical postprocessing of the experimental raw data. Positions of pins and specular echoes in this picture correspond to the experimental data, edges of cavities are defined reasonably well. It means that the basic postprocessing steps are correct. A complete pixel-to-pixel coincidence may be achieved by the application of additional filters that adjust brightness and contrast levels. However, achieving such coincidence is beyond the scope of this paper.

Figure 8c presents the B-scan reconstructed by the numerical postprocessing of the simulated raw data which account bright pins only. The lack of tiny background reflectors results in the lack of the speckled grey background.

Figure 8d presents the B-scan reconstructed by the numerical postprocessing

of the simulated raw data which account both pins and background reflectors in the gel. The addition of the background reflectors makes cavities filled with fluid visible. Specular echoes (small bright dots at the tops and bottoms of the cavities) are not visible due to the features of the current ray tracing implementation. To obtain the response with both specular and speckled echoes at the cavities, more elaborated versions of ray tracing should be developed. This will allow us to simulate scattered echoes in heterogeneous media with complex rheology.

4. Conclusions

The present study is devoted to verification of the numerical model of medical ultrasound [3]. The direct comparison of simulation results with the response recorded in the experiment shows that the numerical model reproduces raw signals on receivers with an acceptable accuracy.

The model can be used for improving quality of medical image reconstruction from ultrasound echo response. The simulated raw data can be used as the input for the image reconstruction postprocessing pipeline to study complex cases and to improve imaging algorithms.

Further development of the numerical model is based on the equations of elasticity for the bone tissues which take into account shear waves [13] that may significantly distort the resulting B-scan image.

References

1. C. D. Arvanitis, G. T. Clement, and N. McDannold, Transcranial assessment and visualization of acoustic cavitation: modelling and experimental validation. *IEEE Trans. Med. Imaging* **34** (2015), No. 6, 1270–1281.
2. S. I. Baskakov, Radio engineering circuits and signals: Textbook for high schools. *M.: Vysshaya Shkola*. 1988 (in Russian).
3. K. A. Beklemysheva, A. A. Danilov, G. K. Grigoriev, A. O. Kazakov, N. S. Kulberg, I. B. Petrov, V. Yu. Salamatova, Yu. V. Vassilevski, and A. V. Vasyukov, Transcranial ultrasound of cerebral vessels in silico: proof of concept. *Russ. J. Numer. Anal. Math. Modelling* **31** (2016), No. 5, 317–328.
4. L. A. Frizzell, E. L. Carstensen, and J. F. Dyro, Shear properties of mammalian tissues at low megahertz frequencies. *J. Acoust. Soc. Amer.* **60** (1976), No. 6, 1409–1411.
5. Gammex 1430 LE phantom User's Guide, http://test.gammex.netphoria.com/ace-files/manuals/1430_usermanual.pdf
6. J. Gu and Y. Jing, Modelling of wave propagation for medical ultrasound: a review. *IEEE Trans Ultrason Ferroelectr. Freq. Control* **62** (2015), No. 11, 1979–1993.
7. A. Kyriakou, E. Neufeld, B. Werner, G. Szkely, and N. Kuster, Full-wave acoustic and thermal modelling of transcranial ultrasound propagation and investigation of skull-induced aberration correction techniques: a feasibility study. *J. Therapeutic Ultrasound* **3** (2015), No. 11. DOI:10.1186/S40349-015-0032-9.
8. E. L. Madsen, H. J. Sathoff, and J. A. Zagzebski, Ultrasonic shear wave properties of soft tissues and tissuelike materials. *J. Acoust. Soc. Amer.* **74** (1983), No. 5, 1346–1355.

9. T. D. Mast, L. M. Hinkelman, L. A. Metlay, M. J. Orr, and R. C. Waag, Simulation of ultrasonic pulse propagation, distortion, and attenuation in the human chest wall. *J. Acoust. Soc. Amer.* **106** (1999), No. 6, 3665–3677.
10. N. Rawlinson, J. Hauser, and M. Sambridge, Seismic ray tracing and wavefront tracking in laterally heterogeneous media. *Advances in Geophysics.* **49** (2008), 203–273.
11. A. B. Sergienko, Digital signal processing. *St. Petersburg.* 2006 (in Russian).
12. N. M. Tole and H. Ostensen, *Basic Physics of Ultrasonographic Imaging.* World Health Organization, 2005.
13. P. J. White, G. T. Clement, and K. Hynynen, Longitudinal and shear mode ultrasound propagation in human skull bone. *Ultrasound Med. Biol.* **32** (2006), No. 7, 1085–1096.